



Starch Grafted Pyrolusite Composite for Enhanced Removal of Malachite Green from Water and Wastewater

Jhilirani Mohanta · Atif Qaiyum ·
Priyanka Priyadarsini Samal · Banashree Dey ·
Subhashri Dutta · Soumen Dey

Received: 3 May 2023 / Accepted: 12 December 2023 / Published online: 3 January 2024
© The Author(s), under exclusive licence to Springer Nature Switzerland AG 2024

Abstract Fabrication of polysaccharide-supported metal oxide composites is effective in eliminating aqueous contaminants including dyes. Herein, a starch-fabricated pyrolusite (SFP) composite was successfully synthesized by copolymerization-induced grafting of starch with pyrolusite and was tested to remove malachite green (MG) dye from water. Here, sodium dodecyl sulfate (SDS) was used for cross-linker with pyrolusite, and ammonium persulfate (APS) was instrumental for grafting initiator with starch and pyrolusite. The synthesized SFP was obtained as a dark brown powder and was analyzed by powder XRD, SEM, BET surface area, pH_{zpc} , HRTEM, and FTIR. An excellent maximum adsorption capacity was found ($170 \text{ mg}\cdot\text{g}^{-1}$) at neutral pH. The adsorption kinetics could be best described by pseudo-second-order and multi-step intra-particle-diffusion model Langmuir isotherm best describes ($R^2=0.999$) the adsorption pathway, suggesting a

monolayer process. The negative thermodynamic parameters suggest a spontaneous (ΔG value -18.893 kJ/mol to -26.635 kJ/mol), endothermic, and feasible process. A high degree of regeneration, (87%), and cyclic reusability is advantageous. A comparison with contemporary adsorbents affirms the efficacy of the material.

Keywords Starch · Pyrolusite · Copolymerization · Grafting · Malachite green · Adsorption

1 Introduction

In the last two to three decades, it has witnessed an increased use of various dyes in diverse segments. As a result, water bodies along with the surrounding environment are facing deterioration. The discharge of organic pollutants including dyes is continuously contaminating water bodies (Jiang et al., 2016). It is well known that dyes are teratogenic, non-biodegradable, mutagenic, noxious, and carcinogenic, in nature. Thus, a need emerges to remove such pollutants using sustainable technologies. The presence of dyes increases the COD and BOD in water, which results in abhorrent smells (Mittal et al., 2018a; Sukriti et al., 2016). Dyes are used in different industries like cosmetics, leather, painting, textiles, paper, and food (Ma et al., 2017; Muthukumaran et al., 2016; Sarmah & Karak, 2020). To remove the hazardous dyes from waterbodies, several techniques have been used such

Supplementary Information The online version contains supplementary material available at <https://doi.org/10.1007/s11270-023-06841-4>.

J. Mohanta · A. Qaiyum · P. P. Samal · S. Dutta ·
S. Dey (✉)
Department of Chemistry, Central University
of Jharkhand, Brambe, Ranchi 835205, India
e-mail: soumen.dey@cuja.ac.in

B. Dey
Department of Chemistry, The Graduate School College
for Women Jamshedpur, Jamshedpur 831001, India

as oxidation, chemical reduction, membrane technology, electrochemical, biological, chemical precipitation, and adsorption (Li et al., 2018a; Noreen et al., 2020; Sharma et al., 2017a). Among all, adsorption is cost-effective and easy to implement (Bhattacharyya et al., 2018; Hosseinzadeh & Ramin, 2018; Naushad et al., 2016). Various nanomaterials (Saad et al., 2017; Sharifpour et al., 2020), nanomaterial-based composite (Moharrami & Motamedi, 2020), graphene oxide (Bhattacharyya et al., 2018), activated carbon, hydrogel (Farag et al., 2018; Junlapong et al., 2020), chitosan (He et al., 2016; Li et al., 2018b), xerogel (Bao et al., 2016), metal oxide, and metal oxide composite (Abdullah et al., 2019) were synthesized and exercised for removal of dyes.

It has been found that in recent years starch-grounded adsorbents are used frequently for their characteristic properties of environmentally friendly, widespread applicability, high sorption capacity, elasticity, thermal resistance, ion exchange capabilities, resistance to microbiological attack, and biodegradability (Farag et al., 2018). Starch has a backbone consisting of free hydroxyl groups on it, and it is a low-cost, very popular compared to chitosan, cellulose, and polysaccharides can be modified easily (Li et al., 2020). Starch-based adsorbents can adsorb dyes primarily through force attraction of hydrogen bonds and weak interaction of Vander Waals forces (Zhang et al., 2020).

Recently, starch-based resins (Zhang et al., 2020), starch-modified ZnMgAl-LDHs (Tao et al., 2018), starch-Pectin magnetite nanoparticles (Nsom et al., 2019), the magnetic nanocomposite based on starch-g-poly (vinyl alcohol) (Pourjavadi et al., 2016), starched silver nanoparticles (Muzaffar & Tahir, 2018), and starch derived zinc-carbon foam-like structure (Priyanka & Saravanakumar, 2018) were reported earlier to remove contaminated dyes from effluents. Enhanced surface area exhibited by the abovementioned adsorbents is the key to successful dye removal.

Starch-fabricated adsorbents such as starch-based nanocomposite (Mallakpour & Rashidimoghadam, 2017), hierarchically porous carbon spheres (Yang et al., 2016), starch/ZnO nanocomposite (Namazi et al., 2019), and starch-coated nanoparticles (Stan et al., 2019) show good adsorption properties. Starch is a nontoxic, biodegradable, cheap polysaccharide, and capable of forming various grafted materials

(Xia et al., 2020). Fabricated starch composites offer a high surface area and porous characteristics, making them ideal adsorbents in the removal of toxic dye molecules (Jiang et al., 2017). Metal oxides significantly contribute to adding higher surface area which is essential to adsorb dye molecules (Mahmoud et al., 2019).

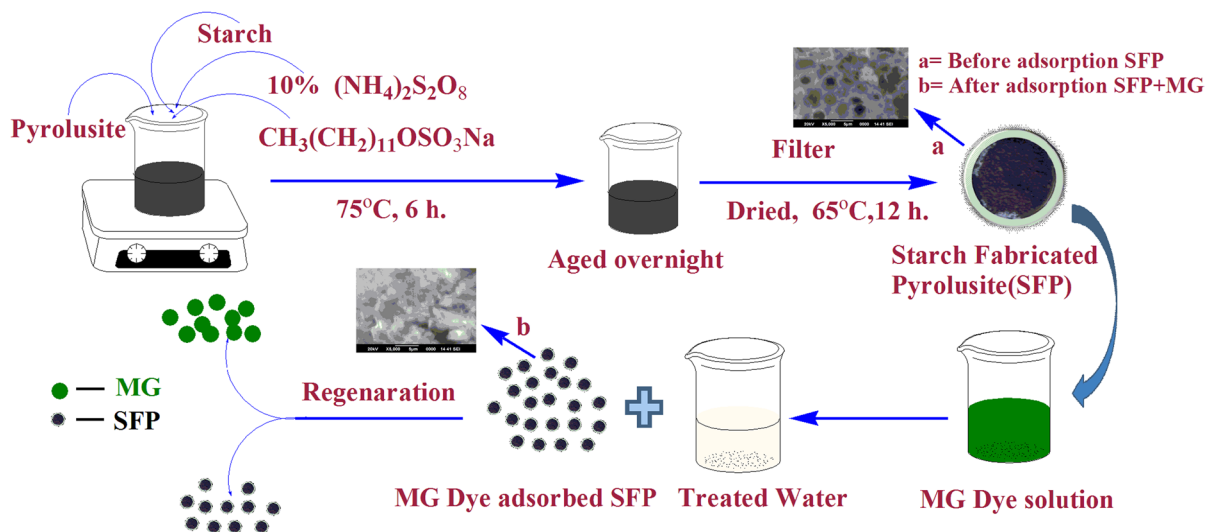
Malachite green is a toxic, non-biodegradable, carcinogenic, and mutagenic dye, so its removal felt necessary from contaminated water (Zare et al., 2018). However, in most cases, efficiency was found moderate and the reusability of the material studied has not been spelled out clearly. In the last couple of years, we have reported the application of several biosorbents (eucalyptus leaf powder, dewaxed honeycomb, mahua seed, activated coconut fiber, coco-peat) and chemisorbents (iron-zirconium binary oxide, cobalt, nickel oxide magnetic nanoparticles) for effective dye treatment from water (Kumari & Dey, 2019; Kumari et al., 2020a, 2020b; Mohanta et al., 2020a, 2020b, 2020c).

With this development, a new starch-fabricated composite material was synthesized by grafting with pyrolusite, a cost-efficient adsorbent on the way to scavenge malachite green. To evaluate the efficiency of starch fabricated pyrolusite (SFP) material, batch experiments have been systematically conducted by changing the various conditions (dose, temperature, concentration, contact time, and pH) effect on it with MG dye. The material was thoroughly characterized by various techniques to establish its efficiency. Thus, SFP is used as a sustainable adsorbent, for dye decontaminate (malachite green) from filthy water.

2 Experimental Section

2.1 Materials and Methods

Starch was bought from Merck, India. Ammonium persulfate (APS) was purchased from Hi-Media chemical private limited, India. Pyrolusite was purchased from Research-Lab Fine Chem Industries (India). The pyrolusite appeared black and amorphous. The elemental composition suggests the presence of Mn-oxide (MnO + MnO₂) content is ~78%. Besides, Fe-oxide (~20%) and Ca-oxide (~2%) were found to be present. Sodium dodecyl sulfate (SDS) was purchased from Research-Lab Fine Chem Industries. Malachite green (MG), sodium chloride (NaCl),



Scheme 1 Flowsheet of the synthesis, adsorption, and regeneration process

sodium hydroxide (NaOH), and hydrochloric acid (HCl) were received from Rankem, India. Each solution used for the experiment was prepared using deionized water. Experiments were conducted in three sets for each investigation. Chemical purity has been presented in the supporting information section (Table S1).

2.2 Characterization

SFP was systematically analyzed by techniques such as FTIR, SEM, XRD (powder), zero-point charge (pH_{ZPC}), surface area (BET), and HRTEM. SEM morphology was recorded in JSM-6390LV instrument, Jeol, Japan. FTIR spectra were documented (IR-Prestige 21 spectrophotometer), in Shimadzu, Japan. Powder XRD was recorded in AXRD proto bench top, Canada, using Cu target at 30 kV and 20 mA. MG dye solution concentrations were measured in Spectrophotometer (Hitachi, U-2900, Japan, double beam UV-Visible) and was used for absorbance study at $\lambda_{\text{max}} = 618 \text{ nm}$. HRTEM of SFP materials was recorded using JEOL, JEM-2100 microscope, Japan. BET surface area was analyzed in Micromeritics 3Flex analyzer instrument. Each batch experiment was carried out in a rotary orbital shaker, Sohag, India. Solution pH and pH_{ZPC} were estimated by Systronics digital pH meter (model 802, India). For

centrifugation, Remi-bench top model R-8 M, India was used to separate adsorbents from the reaction mixture.

2.3 Preparation of Starch Fabricated Pyrolusite

A 5 g pyrolusite was suspended in 100 mL water and stirred in a magnetic stirrer. A 2 g of starch was dispersed into hot water (20 mL, $75\text{--}80^\circ\text{C}$) and slowly added to it. Relatively smaller amylose molecules come out of the starch granules and form a network that holds water, making the mixture viscous which is somewhat analogous to starch gelatinization. To this solution, a 10% ammonium persulfate dissolved in water (20 mL) was added drop-wise as an attaching initiator followed by drop-wise addition of 4 g sodium dodecyl sulfate that was liquefied in water (20 mL). The resultant mixture was heated (75°C) for 6 h with constant stirring. A thick dark brown precipitate gradually started to form. To eliminate unreacted starch, APS, and SDS, the precipitate has been washed with warm water several times. The material was aged overnight, filtered through G-4 frit (Zenith glass, 5–15 microns size, 80 mL), washed thoroughly with hot water, and dried at 65°C in a hot air oven for 12 h. Yield is 84%, and appearance is amorphous powder. The scheme of the reaction is provided in the supporting information section (Scheme S1). A flowsheet of the process was provided as Scheme 1.

3 Experimental

3.1 Dye Adsorption Study

All experiments were carried out using non-corrosive plastic bottles in a triplicate set. In a typical experimental setup, dye solutions (50 mL) have been taken with different concentrations (10–100 mg/L), a time interval (5–140 min) was fixed at different pH (3–9), and adsorbents were added at a different dose (0.05–0.5 g). All the bottles were sealed by teflon and agitated at a shaking speed (120 ± 5 rpm) at room temperature (298 K). After completion of the desired experiment, the residual solution was centrifuged at 5000 ± 5 rpm for 3 min, SFP particles were separated, and residual the dye concentration was measured. The maximum adsorption capacity and adsorption percentage at equilibrium were estimated using the following Eqs. (1–2):

$$q_e = (C_0 - C_e) \times \frac{V}{m} \quad (1)$$

$$R\% = \left(\frac{C_0 - C_e}{C_0} \right) \times 100 \quad (2)$$

where q_e is for dye adsorption capacity in mg.g^{-1} at equilibrium and C_0 and C_e denote the concentration of MG dye (mg.L^{-1}) solution at the initial and final stages, respectively. V is the volume of MG dye solution used (mL). m (g) is the weight of SFP used, and $R\%$ is the percentage of adsorption. Estimation of pH_{zpc} was done by using the solution drift method with the standard procedure reported in the literature.

3.2 pH_{zpc} estimation

The pH drift method was used for the zero-point charge measurement of the SFP adsorbent. Stock solutions (0.01 M NaCl in 500 mL) were prepared; SFP (100 mg) was added to NaCl (50 mL, stock solution), with different pH ranges from 2 to 12. The solution was shaken for 22 h at 110 ± 5 rpm, and the final pH (NaCl solution) was estimated. It was found that 6.71 was evaluated pH_{zpc} (by plotting initial and final pH).

3.3 Regeneration

The regeneration study was carried out with three different stripping agents: 0.1 M of sodium hydroxide, 0.1 M of hydrochloric acid, and 0.1 M of sodium chloride. Dye-loaded SFP composite adsorbent was washed with distilled water for the removal of surface-adhering dye molecules. It was then dried and mixed with each of the disrobing solutions and was shaken for 4 h. SFP composite adsorbents were separated using a centrifuge, and residual dye concentrations were measured. Regenerated material was washed, dried, and tested for reuse. Cyclic efficiency was measured as follows:

$$\text{Efficiency}(\%) = \left(\frac{\text{dye uptake in second run}}{\text{dye uptake in first run}} \right) \times 100$$

4 Results and Discussions

4.1 Characterization

4.1.1 FTIR

FTIR analysis and spectra for SFP with SFPMG are presented in Fig. 1a. The peak of 3421 cm^{-1} is attributed to O–H stretching frequency for SFP which after MG adsorption gets shifted to 3406 cm^{-1} . It is dependable on prior reports (Haq et al., 2020; Irinislimane & Belhaneche-Bensemra, 2017; Liu et al., 2016). The peak showing at 3042 cm^{-1} corresponds to the C–H stretching frequency (aromatic) of MG dye. The sharp peak indicated at 2926 cm^{-1} is responsible for the aliphatic C–H stretching of starch. After adsorption, one additional peak was identified at 2917 cm^{-1} which is due to C–H stretching of MG (Mohanta et al., 2019; Sharma et al., 2017). This confirms successful dye adsorption. The sharp peaks are present at 1595 cm^{-1} , and the small peak at 1575 cm^{-1} corresponds to N–H stretching after the adsorption of MG (Haq et al., 2020; Irinislimane & Belhaneche-Bensemra, 2017; Jiang et al., 2017; Kumari & Dey, 2019; Kumari et al., 2020a, 2020b; Liu et al., 2016; Mahmoud et al., 2019; Mallakpour & Rashidimoghadam, 2017; Mohanta et al., 2020a,

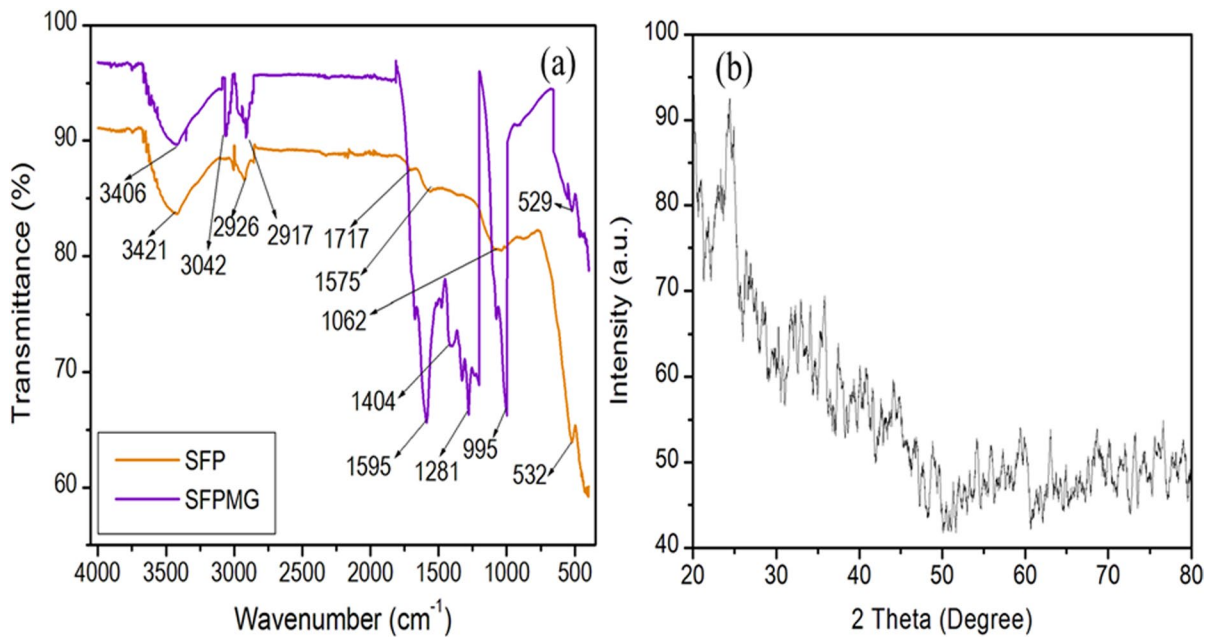


Fig. 1 **a** FTIR spectra of SFP before adsorption (yellow line) and onto SFPMG, after adsorption (purple line). **b** XRD spectrum of SFP

2020b, 2020c; Muzaffar & Tahir, 2018; Namazi et al., 2019; Nsom et al., 2019; Pourjavadi et al., 2016; Priyanka & Saravanakumar, 2018; Sharma et al., 2017; Stan et al., 2019; Tao et al., 2018; Xia et al., 2020; Yang et al., 2016; Zain et al., 2018; Zare et al., 2018). The weak band at 1404 cm^{-1} corresponds to C–O–H bending vibration. The broad band at 995 cm^{-1} is for C–O bending vibration (Haq et al., 2020; Sonawane & Patil, 2018; Su et al., 2018). Peaks showing at 532 and 529 cm^{-1} are endorsed to Mn–O stretching originating from pyrolusite before and after dye treatment. This indicates the involvement of oxygen in the binding of dye through various interactions.

4.1.2 XRD Analysis

Figure 1b indicates the demonstration of powder XRD meant for SFP composites adsorbent. The amorphous nature was identified with weak diffraction peaks. The peak at 24.5° and 63.4° is due to the pyrolusite unit. Other peaks were not found prominent probably due to the embedding of pyrolusite within the starch macromolecular framework.

4.1.3 SEM Analysis

Figure 2a indicates the surface morphology of SFP identified by SEM analysis. It was seen from the microphotograph that the SFP is highly porous having tetragonal, pentagonal, and hexagonal pores. Such pores facilitate the adsorption of dye more efficiently. From Fig. 2b, it was observed that pores are mostly occupied by MG dye leaving almost no pores behind on the surface. An agglomerated, condensed surface was seen with blocked pores. SEM images were found to be fully conducive to ascertain the texture and dimensions of the SFP particles. Therefore, HRTEM was recorded which shows some oval-shaped geometries. Figure 2c shows the HRTEM image of SFP. It was seen that the particle dimensions are well in the nanoscale range, which justifies the excellent adsorption capacity. The hexagonal nature of the particle texture could be identified as well.

4.1.4 BET Surface Area Analysis

Figure 2d presents the BET plot of SFP. The BET surface area was obtained $181.354\text{ m}^2/\text{g}$, indicating

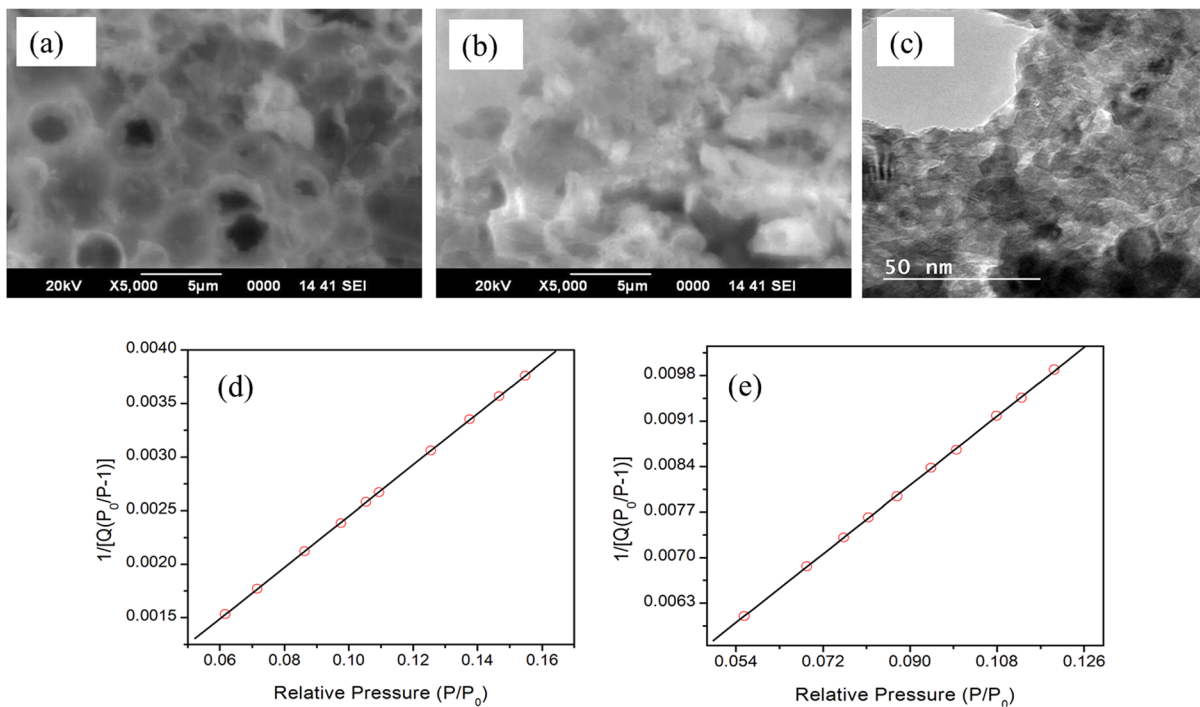


Fig. 2 SEM pictures: **a** SFP before adsorption MG, **b** SFP after adsorption of MG, **c** HRTEM image of SFP, **d** SFP and BET surface area, **e** BET surface area after MG adsorption

that the material is highly porous leading to prominent and favorable adsorption of MG onto SFP surface. Table S2 represents a comparative illustration of the surface area of different adsorbents. After the adsorption of MG dye, the BET surface area was obtained $70.656 \text{ m}^2/\text{g}$ (Fig. 2e), confirming about a 62% reduction in surface area. It indicates the predominant adsorption of MG dye onto the surface of SFP.

4.2 Dye Adsorption Study

4.2.1 Effect of Contact Time

The adsorption process is divided into three phases: rapid, slow, and dynamic equilibrium phase. The effect of contact time is shown in Fig. 3a. Initially, adsorption was found to have rapid growth, within 10 min more than 50% of adsorption took place. The overall uptake process seems to be uniform, and it becomes slower upon increasing the time, and eventually, the equilibrium time was reached within 120 min. Initially, the number of the available

surface (vacant sites) is more on the SFP adsorbent outward, and dyes get adsorbed readily. With time, saturation of pores coupled with intermolecular repulsion hinders the adsorption profile. Hence, for all other experiments, an agitation time of 120 min was chosen (Sharma et al., 2017; Sharma et al., 2017c).

4.2.2 Effect of pH

Figure 3b displays the pH effect, and Fig. 3e shows the estimation of pH_{zpc} of SFP. pH_{zpc} , as assessed by the drift method, was found at $6.71 \text{ pH}_{\text{zpc}}$ (Fig. 3e). At $\text{pH} < 6.71$, the surface of SFP was positively charged. At $\text{pH} > 6.71$, the surface of SFP is negatively charged. pH variation was carried out in the range 3–9. At pH 3, adsorption is only 30%, and with increasing pH, there is a steady increase up to 90% at pH 8. At lower pH, the solution is enriched with proton, and the surface of the adsorbent (SFP) is positively charged. This result, between cationic dye (MG) and the positive surface of SFP, is the electrostatic force of repulsion, leading to lower adsorption.

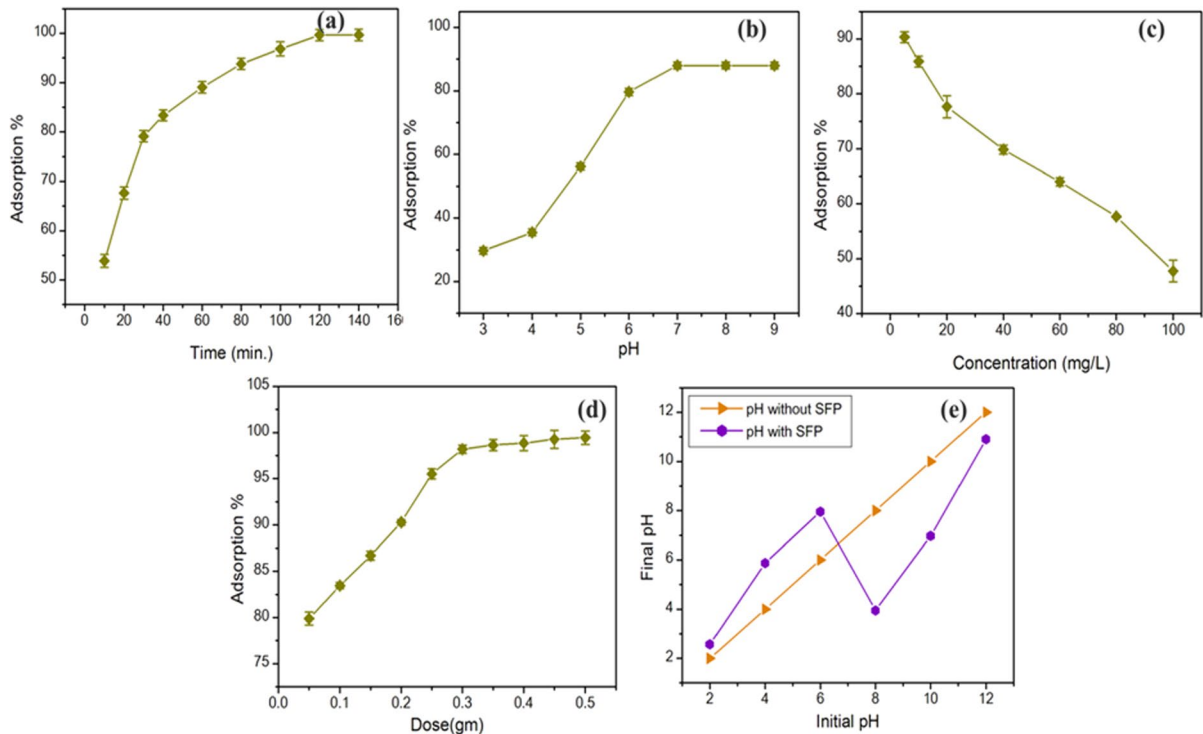


Fig. 3 Batch experiments: **a–d** contact time, pH concentration, and dose–effect respectively. **e** pH_{zpc}

In addition, there is a competitive inhibition from a proton-enriched environment which reduces the adsorption percentage. Above pH 6.71, the generation of a negatively charged surface facilitates cationic dye-binding through electrostatic attraction. However, above pH 8, no more adsorption was seen up to pH 9. This may be attributed to two factors. The first is the saturation of available active sites, while the other is structural changes of MG at a highly alkaline medium. Figure 3b confirms that pH 7 is the best for adsorption. This is the additional advantage of SFP, and it can be used in real sample analysis. It works well in drinking water pH and can tolerate interference from other ions without compromising its actual performance (Supporting information section Fig. S1).

4.2.3 Effect of Initial Dye Concentration

Concentration effects were measured by varying different concentrations from 10 to 100 mgL^{-1} . Figure 3c shows that with an increasing concentration range from 10 to 100 mgL^{-1} , the adsorption

percentage decreases from 91 to 48%. This is due to the difference in concentration of the dye solution diffusing to the SFP surface decreases, and also decreasing the driving force which is obligatory for mass transfer from MG dye (solution phase) to the solid phase (SFP). Moreover, intermolecular repulsion among dye molecules hinders effective binding, which affects the adsorption; gradually decreases (Sharma et al., 2016a, 2016b, 2018b, 2019).

4.2.4 Effect of Adsorbent Doses

Figure 3d illustrates variation for adsorption with increasing adsorbent (SFP) dose (0.05–0.5 g). The percentage of adsorption increased from 79.5% to 98.7%. This is due to the higher availability of pores. Above a dose of 0.25 g, adsorption turns out to be almost constant. The progress of the adsorption percentage onto SFP is for an increase in the approachability of active (SFP) sites on the adsorption of MG dye molecules (Azzaz et al., 2016, 2017, 2018). A similar observation was seen earlier (Irinislimane & Belhaneche-Bensemra, 2017).

4.2.5 Effect of Coexistent Ions

Common industrial wastewater/effluent invariably contains a mixture of many ions used in the form of salts, and/or binders. In some cases, heavy metals may also accompany dyes in such effluent. Also, groundwater/surface water/industrial effluent by nature contain ions such as chloride, phosphate, arsenate, nitrate, and calcium in different concentrations. Such ions were mixed in the simulated dye solution to test their relative perturbation to the adsorption efficiency. Concentrations of such ions were chosen as per the maximum permissible limit as specified by WHO (Shehzad et al., 2019). According to WHO, the permissible limits for nitrate (10 mg.L⁻¹), chloride (200 mg.L⁻¹), sulfate (200 mg.L⁻¹), phosphate (50 mg.L⁻¹), and arsenate (0.05 mg.L⁻¹). Solutions of aforesaid strengths were prepared, and relative interference was investigated. Results are presented in Fig. S1 (Supporting information). Fig. S1 demonstrates the individual effects of interference. It was found that the presence of co-existent ions decreases the adsorption percentage by 8–22% depending upon the nature of the ions.

4.3 Adsorption Kinetics

To understand the mode of adsorption on SFP, kinetics models play an important role. The mass transfer mechanism has a guiding role to provide insight into the rate of adsorption. Four kinetics models, namely, pseudo 1st order, 2nd order, pseudo 2nd order, and intra-particle kinetic models, were investigated (Sonawane & Patil, 2018; Zain et al., 2018). At the time of adsorption, firstly, MG molecules drift from the solution onto the SFP adsorbent surface through the process, namely, the boundary layer followed by the mass transfer via internal pore diffusion. The pseudo 2nd order kinetic model indicates the quantity of MG dye adsorbed on the SFP surface (Hashem et al., 2007; Hosseinzadeh & Ramin, 2018; Pourjavadi et al., 2016).

$$\log(q_e - q_t) = \log q_e - \left(\frac{k_1}{2.303} \right) \cdot t \quad (3)$$

$$t/q_t = 1/(k_2 \cdot q_e^2) + t/q_e \quad (4)$$

$$q_t = k_{id}t^{0.5} + C \quad (5)$$

$$1/(q_e - q_t) = 1/q_e + k_1 \cdot t \quad (6)$$

where q_e and q_t (mg.g⁻¹) are the amounts of MG adsorbed at equilibrium and at different times t (min) respectively. The k_1 (min⁻¹), k_2 (g.mg⁻¹.min⁻¹), k_{id} (mg.g⁻¹.min^{-0.5}), and k_t are rate constant of the pseudo-first order, pseudo-second order, intra-particle diffusion, and second order respectively. C is the boundary layer thickness.

By plotting $\log(q_e - q_t)$ vs t (pseudo 1st), t/q_t vs t (pseudo 2nd), q_t vs $t^{1/2}$ (intra-particle diffusion), and $1/(q_e - q_t)$ vs t (2nd order), respective values of four kinetic constants were obtained (Fig. 4a–d).

The first-order model does not fit properly for the data obtained and could be considered only for the initial phase of adsorption. It was found that the pseudo-second-order model is the best fit ($R^2=0.999$). This suggests that the adsorption involves chemisorption as a rate-determining step, originating from the electrostatic interaction of the dye and the SFP. A similar observation was found earlier. The intra-particle diffusion plot seems divided into three characteristic linear regions (Fig. 4c). A close inspection of the intra-particle model reveals that there are indeed three different slopes of three stages of adsorption (Supporting information, Fig. S2). Initially, (0–35 min) adsorption was found rapid signifying that it occurs through film diffusion, indicating external mass transfer, which involves the transportation of MG dye from the bulk liquid phase to the solid phase of SFP. A steep upward slope confirms the rapid uptake of MG dye molecules onto the SFP surface. After that, the second curve could be recognized (35–90 min.) through pore diffusion, and the third region lies at a higher contact time (90–140 min), displaying continuing adsorption stage which is dominated by the pore diffusion (Shehzad et al., 2019). Selected kinetic constants are presented in Table 1.

4.4 Adsorption Isotherm

The adsorption isotherm defines the interaction between the SFP adsorbent and MG adsorbate molecules at equilibrium. Four isotherm models, namely, Langmuir, Temkin Freundlich, and the D-R model,

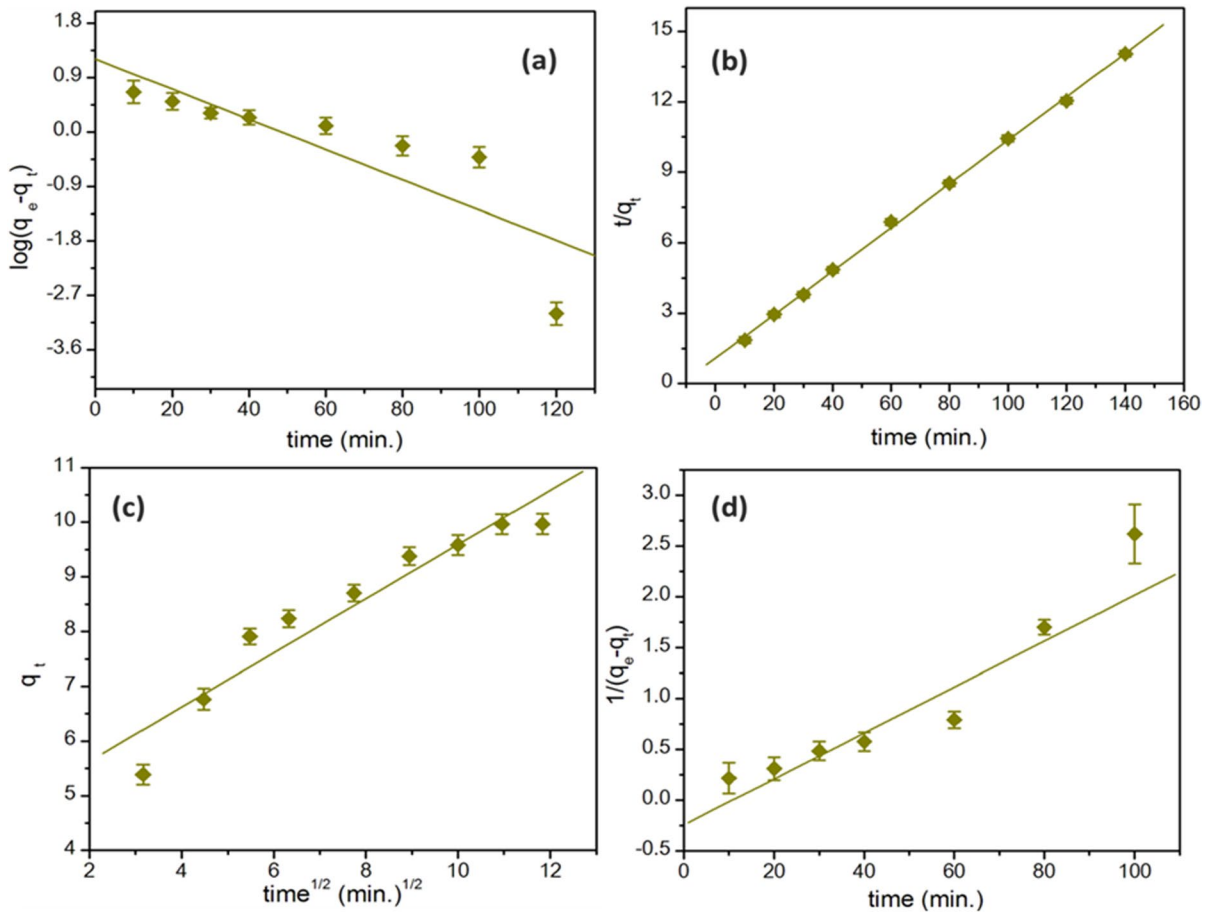


Fig. 4 Kinetic studies: **a–d** pseudo 1st order, pseudo 2nd order, intra-particle diffusion, and 2nd-order plots, respectively

Table 1 Parameters (kinetics) for the adsorption of MG dye onto SFP

Kinetic model	q_e (mg/g)	K (kinetic constants)	R^2
Pseudo first order	9.781	$k_1=0.057$	0.841
Pseudo second order	17.129	$k_2=0.007$	0.999
Second order	3.523	$k_1=0.025$	0.908
Intra-particle diffusion	4.644	$k_{id}=0.494$	0.914

were chosen for the present study. Langmuir’s model defines monolayer and homogeneous adsorption, whereas Freundlich defines multilayer and heterogeneous adsorption (Amode et al., 2016; Bhatti et al., 2020; Dey et al., 2021). Equation (7) indicates the Langmuir model (linear):

$$\frac{C_e}{q_e} = \frac{1}{K_l q_{max}} + \frac{C_e}{q_{max}} \tag{7}$$

Dimensionless equilibrium/separation factor R_L is evaluated by Eq. (8):

$$R_L = \frac{1}{(1 + bC_0)} \tag{8}$$

where C_e (mg.L⁻¹) is the equilibrium concentration, q_e (mg. g⁻¹) is the amount of dye adsorbed per unit mass of the adsorbent at equilibrium, q_{max} (mg. g⁻¹) represents the maximum monolayer adsorption capacity per unit mass of adsorbent, and K_l is the Langmuir affinity constant (L.gm⁻¹). The value of q_{max} and K_l (L.mg⁻¹) was calculated from the slope and intercept (C_e vs C_e/q_e) shown in Fig. 5a. Constant b (L. mg⁻¹) relates to the heat of adsorption.

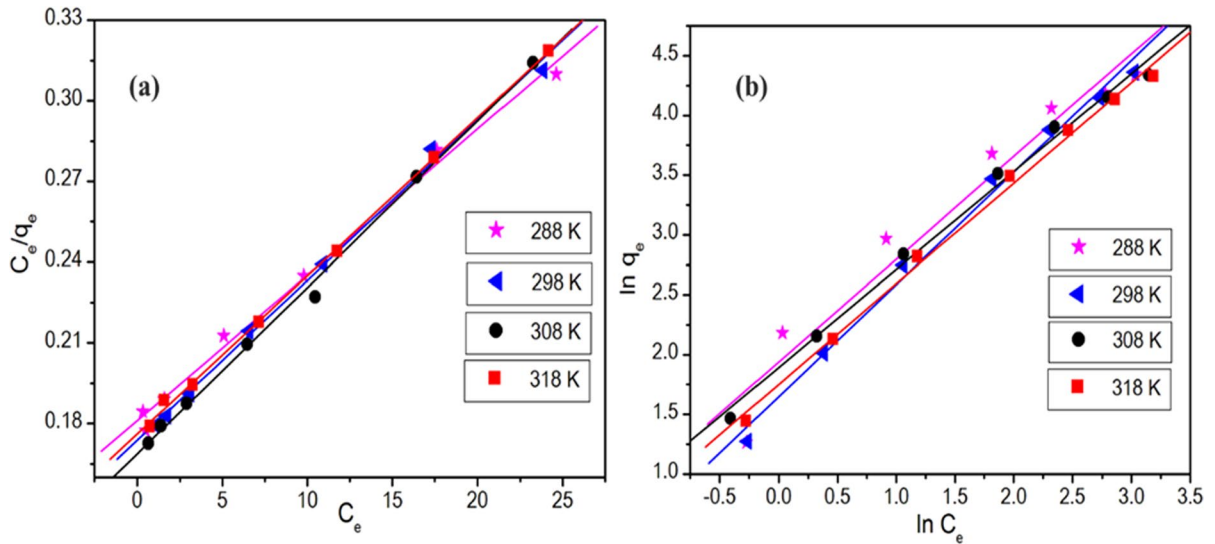


Fig. 5 Isotherm models: **a** Langmuir model and **b** Freundlich model

The linear form of Freundlich equation is given by Eq. (9):

$$\ln q_e = \frac{1}{n} \ln C_e + \ln K_f \tag{9}$$

where K_f is the Freundlich constant related to the adsorption capacity of the adsorbent and n indicates the type of isotherm and the adsorption intensity of the adsorbent. When $1/n < 1$, it represents a chemical process operating in adsorption (Mittal et al., 2018b; Sharma et al., 2017b; Xing et al., 2012). By plotting $\ln q_e$ against $\ln C_e$, respective values of K_f and n were calculated from the intercept and slope (Fig. 5b). The value of $1/n$ lies in the range of 1.18 to 1.327, suggesting little involvement of the Freundlich model.

It is evident from Fig. 5 that the best-fit model: the Langmuir model with a maximum $R^2=0.999$. Corresponding b values lie in the range 0–1 (Table 2),

suggesting a favorable adsorption process (Darwish et al., 2019). The adsorption capacity was found to be $170.068 \text{ mg.g}^{-1}$ at 318 K from the Langmuir model. The correlation coefficient ($R^2=0.999$) also strongly supports for Langmuir model (Table 2). With increasing temperature, the maximum adsorption capacity of MG onto SFP was found to increase from 123 to 170 mg.g^{-1} . This suggests that adsorption is favorable at higher temperatures. The intermolecular forces between adsorbent and adsorbate are much stronger than between the solvent and adsorbate at elevated temperatures. As a result, increasing temperature causes adsorbate to get adsorbed easier and diffuse inside.

The Temkin model shows homogeneous multivalent interactions. The Temkin model describes the uniform binding of adsorbate-adsorbent (Zhang et al., 2017). The Temkin model is given in Eq. (10):

Table 2 Selected isotherm constants for the adsorption of MG onto SFP

Temperature (K)	Langmuir isotherm				Freundlich isotherm		
	q_{\max} (mg.g-1)	b (L.mg-1)	R_L	R^2	K_f (mg/g)(L/mg) ^{1/n}	n	R^2
288	123.267	0.082	0.549	0.993	9.328	1.327	0.951
298	144.101	0.065	0.606	0.996	7.508	1.276	0.945
308	152.439	0.044	0.694	0.997	6.639	1.221	0.937
318	170.068	0.033	0.751	0.999	5.756	1.187	0.918

$$q_e = B_1 \ln K_T + B_1 \ln C_e \tag{10}$$

$$B_1 = RT/b \tag{11}$$

where B_1 is the Temkin constant. K_T is an equilibrium binding constant ($L \cdot gm^{-1}$), and K_T and B_1 can be obtained by plotting q_e versus $\ln C_e$, from the intercept and slope (Fig. S4a, Supporting information).

Dubinin-Radushkevich (D-R) isotherm assumes the adsorption equilibrium for the interaction of the adsorbate-adsorbent onto the microspore size of the adsorbent (Zhang et al., 2011). Equation (12) enlightens the linear form of D-R isotherm:

$$\ln q_e = \ln q_s - B \varepsilon^2 \tag{12}$$

$$\varepsilon = RT \ln(1 + (1/C_e)) \tag{13}$$

$$E = 1/\sqrt{2B} \tag{14}$$

where q_s ($mol \cdot gm^{-1}$) is the D-R constant. B is the mean of free energy (E , $kJ \cdot mol^{-1}$) of the adsorption in terms of energy (Eq. 14) per molecule. Plotting ε^2 against $\ln q_e$ the intercept and slope gives the value of q_s and B , respectively (supporting information, Fig S4b).

Temkin and D-R model data have been presented in Table S3 (supporting information). From the table,

it is confirmed that the adsorption of MG onto SFP follows Temkin at higher temperatures along with the Langmuir adsorption model. The corresponding correlation coefficient value is 0.989.

4.5 Adsorption Thermodynamics

The thermodynamic investigation was carried out to evaluate the change in free energy, enthalpy, and entropy that occurred during the adsorbent-adsorbate interaction. Gibbs free energy (ΔG) indicates the feasibility of adsorption on SFP and MG interaction and is evaluated by the following Eqs. (15)–(17) (Sharma et al., 2018a):

$$\Delta G^\circ = -RT \ln K \tag{15}$$

Using the following Van't Hoff (Eq. (16)), change in entropy (ΔS), and enthalpy (ΔH) can be calculated. Relevant equations are given (Eq. (16)–(17)) (Fig. 6b):

$$\ln K = \frac{\Delta S}{R} - \frac{\Delta H}{RT} \tag{16}$$

$$k = \frac{q_e}{c_e} \tag{17}$$

where R is the universal gas constant ($R=8.314 \text{ J mol}^{-1} \text{ K}^{-1}$). Van't Hoff plot of $\ln K$

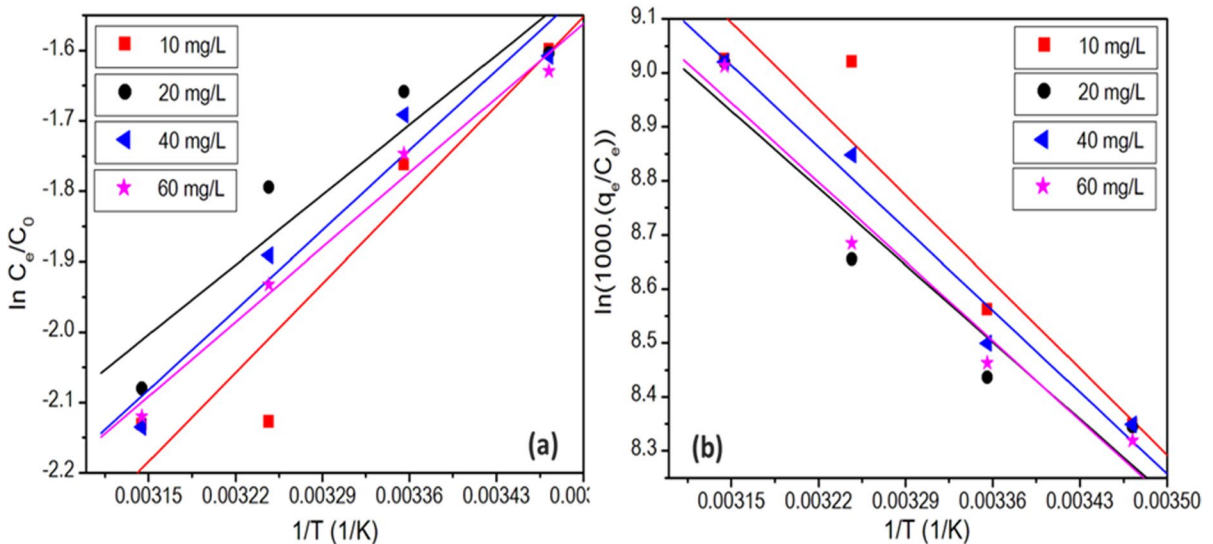


Fig. 6 a Arrhenius plot (MG onto SFP), b Van 't Hoff plot (MG onto SFP)

against $1/T$ entropy, enthalpy, and free energy change was calculated from the slope and intercept.

The negative value of ΔG ($\sim 20 \text{ kJ.mol}^{-1}$) suggests feasible and spontaneous adsorption. Positive values of ΔH indicate that the adsorption of MG onto SFP is endothermic, whereas the positive value of ΔS indicates increased randomness at the solid and solution junction during the adsorption process (Table 3).

Activation energies provide an important clue about the nature of an adsorption process, and the Arrhenius equation allows the calculation of activation energies involved therein. Figure 6a presents the Arrhenius plot of MG onto SFP. The activation energy values for various concentrations (10, 20, 40, and 60 mg.L^{-1}) are 7.988, 10.709, 12.580, and 16.588 kJ.mol^{-1} , respectively. This is also consistent with Fig. 3c. Such values specify that the adsorption process lies in between physisorption and chemisorption. (Zhou et al., 2019).

4.6 Regeneration and Reusability

An adsorption process stands economical and sustainable when the spent adsorbent can be regenerated and reused for sufficient time and a good number of cycles (Dey et al., 2022; Qaiyum et al., 2022). Here, the dye-loaded SFP was tested for regeneration with three different eluents such as sodium hydroxide (0.1 M), sodium chloride (0.1 M), and hydrochloric acid (0.1 M). It was seen that the best regeneration was achieved with HCl (87%). This can elucidate by the exchange of binding sites with the MG dye molecules with H^+ ions. Though a paltry regeneration was seen for NaOH (7%) and NaCl (11%), these are insignificant for further use of the material. Figure 7a presents the regeneration using various stripping solutions. Upon successful regeneration, the material was employed for consecutive adsorption–desorption cycles. It was seen that SFP can be used for up to five

cycles (Fig. 7b) without losing significantly. Thereafter, efficiency of the adsorbent becomes insignificant. Such a situation creates a waste disposal problem. Currently, we are working on the acid-digestion-based decomposition of dye-laden material for providing a solution for the same.

4.7 Mechanism of Dye Adsorption onto SFP

The chemical interactions operating within the system influence the dye adsorption mechanism of the adsorbate into the adsorbent surface. Different functional groups (hydroxyl, alcohol, aldehyde) can be easily acquainted with the starch spine to improve the adsorption performance for metal ions and various dyes through some specific interactions such as electrostatic interaction, H-bonding, and chelating effects (Li et al., 2018a). When the SFP adsorbent is added to the MG dye solution, the dye molecules get attached to the surface of the SFP adsorbent through the electrostatic force in between cationic dye (MG) and negatively charged SFP, van der Waal force of attraction, and pi–pi interaction (Fig. S3, supporting information); SFP adsorbent shows some characteristic peaks in FTIR before and after adsorption that confirms the binding of MG with SFP. This is consistent with our earlier results (Dey et al., 2007, 2022).

4.8 Analysis of Industrial Effluent

Simulated batch experiments become more important and meaningful when it is extrapolated to industrial effluent analysis. For this purpose, a real sample was collected from a nearby textile dyeing unit. The obtained sample was received as intensely colored along with some suspension-like appearance. It was centrifuged thrice for 10 min at 4000 rpm, and the clear solution thus obtained was first diluted with a

Table 3 Thermodynamic parameters for the adsorption of MG onto SFP

C_0 (mg/L)	ΔH^0 (kJ/mol)	ΔS^0 (kJ/mol.K)	ΔG^0 (kJ/mol)			
			288 K	298 K	308 K	318 K
10	24.563	0.161	– 21.805	– 23.415	– 25.025	– 26.635
20	17.945	0.129	– 19.207	– 20.497	– 21.787	– 23.077
40	15.797	0.121	– 19.051	– 20.261	– 21.471	– 22.681
60	14.515	0.116	– 18.893	– 20.053	– 21.213	– 22.373

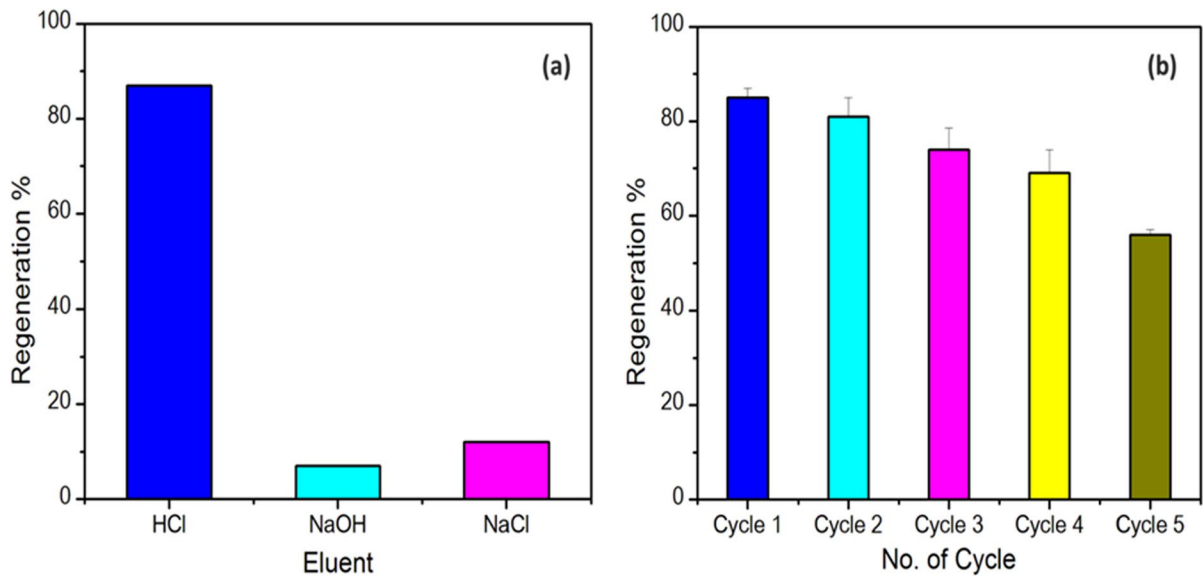


Fig. 7 a Regeneration of SFP using various stripping solutions. b Efficiency estimation in continuous adsorption–desorption cycles (five cycles)

known volume of water, pH was measured, and initial dye concentration was measured (120 mg/L). Working pH was adjusted before the adsorption study. Thereafter, following the usual batch procedure, 0.5 g SFP was added to effluent (50 mL) and shaken for 120 min, and the residual concentration was measured (55 mg.L^{-1}). A concentration reduction of up to 55% was achieved. From this observation, we can conclude that SFP can be used for the treatment of industrial effluent. When 1 g SFP was used, 81% removal was noted. No more increase was found even doubling the adsorbent amount. It is noteworthy that field effluent may invariably contain other ions which may have partially suppressed the removal beyond 81%.

4.9 Cost Evaluation

We reported the scavenging of malachite green using different low-cost adsorbents such as activated coconut fiber, coco peat, de-waxed honeycomb, eucalyptus leaves, metal oxides nanoparticles, binary and ternary metal oxide, and metal composites prepared. Each of them has its advantages. The preparation of the SFP endeavored to minimize the preparation cost so that the prepared SFP could be commercialized subsequently for field application.

SFP synthesis accounts cost of INR 250.00 only (equivalent to USD 3.06). The material can be reused after regeneration. Costs of the used materials are as follows: APS 5.72 RS/g, strach 2.88 RS/g, pyrolusite 1.94 RS/g, and SDS 12.67 RS/g.

4.10 Comparisons of SFP with Other Adsorbents

To assess the real-time performance of a newly synthesized material, it is important to compare its efficiency with the relevant materials reported earlier. Table 4 summarizes the adsorption efficiency of SFP with other starch-based adsorbents. It was found that barring a few, the present material is superior to the others in terms of adsorption capacity.

5 Conclusions

A starch-fabricated pyrolusite composite was synthesized by the grafting-copolymerization method using pyrolusite in the presence of ammonium persulfate and sodium dodecyl sulfate. The material was isolated in good yield as a water-stable adsorbent and excellent adsorption of MG dye was achieved under ambient conditions. The adsorbent shows oval-shaped and porous surface morphology. The maximum adsorption

Table 4 Comparison of SFP with other adsorbents for dye removal

Adsorbent	Adsorbate	Adsorption capacity (mg.g ⁻¹)	Reference
ST/PL(AA-cl-AAm) NHG	Brilliant blue R-250	31.24	Sharma et al., 2017b)
NHA	Malachite green (MG)	297	Hosseinzadeh & Ramin, 2018)
PSX/MSA	Gardenia yellow (GY)	6.688	Bao et al., 2016)
MNP@St-g-PVS	Malachite green (MG)	567	Pourjavadi et al., 2016)
MCA	Methylene violet (MV)	158.05	Mittal et al., 2018b)
CS/OSR/Silica	Direct Blue 71	67.02	He et al., 2016)
CS/OSR/Silicas	Direct Red 31	94.2	He et al., 2016)
MWCNT-starch	Methyl orange (MO)	135.8	Chang et al., 2011)
MWCNT-starch	Methylene blue (MB)	93.7	Chang et al., 2011)
DMAEMA	Astrazon red (AR)	263	Farag et al., 2018)
Pyrolusite	Malachite green (MG)	33.567	Mohanta et al., 2019)
Starch-fabricated pyrolusite (SFP)	Malachite green (MG)	170.068	Present work

capacity was 170.068 mg.g⁻¹, which is far better than raw pyrolusite (33.567 mg.g⁻¹). The adsorption follows pseudo-second-order along with intra-particle diffusion kinetics. Langmuir isotherm model is following of the adsorption of MG onto SFP. The process is feasible and spontaneous evident from thermodynamic data. Simple regeneration empowers multi-cycle use without significant loss of activity. Industrial effluent was tested for real-time efficiency check and found promising. It can be concluded that the starch-grafted pyrolusite composite can be an ideal choice for dye removal from water.

Acknowledgements The authors thank the Central University of Jharkhand for the infrastructure and institute fellowships to J.M., M.A.Q., P.P.S., and S.D.

Author Contribution J.M.: Experiments, data acquisition, writing original draft. A.Q.: data acquisition. P.P.S.: referencing S.D.: data validation. B.D.: manuscript review, professional editing. S.D.: overall supervision, review and editing, conceptualization.

Data Availability The data used to support the findings of this study are available from the corresponding author upon request.

Declarations

Competing Interests The authors declare no competing interests.

References

- Abdullah, N. H., Shameli, K., Abdullah, E. C., & Abdullah, L. C. (2019). *Composites Part B: Engineering*, 162, 538. <https://doi.org/10.1016/j.compositesb.2018.12.075>
- Amode, J. O., Santos, J. H., Alam, ZMd., Mirza, A. H., & Mei, C. C. (2016). *International Journal of Industrial Chemistry*, 7, 333. <https://doi.org/10.1007/s40090-016-0085-9>
- Azzaz, A. A., Jellali, S., Assadi, A. A., & Bousselmi, L. (2016). *Desalination and Water Treatment*, 57(46), 22107. <https://doi.org/10.1080/19443994.2015.1103313>
- Azzaz, A. A., Jellali, S., Akrouf, H., Assadi, A. A., & Bousselmi, L. (2017). *Environmental Science and Pollution Research*, 24(11), 9831. <https://doi.org/10.1007/s11356-016-7698-6>
- Azzaz, A. A., Jellali, S., Akrouf, H., Assadi, A. A., & Bousselmi, L. (2018). *Journal of Cleaner Production*, 201, 28. <https://doi.org/10.1016/j.jclepro.2018.08.023>
- Bao, L., Zhu, X., Dai, H., Tao, Y., Zhou, X., Liu, W., & Kong, Y. (2016). *International Journal of Biological Macromolecules*, 89, 389. <https://doi.org/10.1016/j.ijbiomac.2016.05.003>
- Bhattacharyya, A., Banerjee, B., Ghorai, S., Rana, D., Roy, I., Sarkar, G., Saha, N. R., De, S., Ghosh, T. K., Sadhukhan, S., & Chattopadhyay, D. (2018). *International Journal of Biological Macromolecules*, 116, 1037. <https://doi.org/10.1016/j.ijbiomac.2018.05.069>
- Bhatti, H. N., Safa, Y., Yakout, S. M., Shair, O. H., Iqbal, M., & Nazir, A. (2020). *International Journal of Biological Macromolecules*, 150, 861. <https://doi.org/10.1016/j.ijbiomac.2020.02.093>
- Chang, P. R., Zheng, P., Liu, B., Anderson, D. P., Yu, J., & Ma, X. (2011). *Journal of Hazardous Materials*, 186, 2144. <https://doi.org/10.1016/j.jhazmat.2010.12.119>

- Darwish, A. A. A., Rashad, M., & Al-Aoh, H. A. (2019). *Dyes and Pigments*, 160, 563. <https://doi.org/10.1016/j.dyepig.2018.08.045>
- Dey, S., Pal, K., & Sarkar, S. (2007). *Tetrahedron Letters*, 48(31), 5481–5485. <https://doi.org/10.1016/j.tetlet.2007.05.168>
- Dey, S., Chakraborty, R., Mohanta, J., & Dey, B. (2022). *Bioremediation Journal*. <https://doi.org/10.1080/10889868.2022.2086530>. in press.
- Dey, S., Bhagat, P., Mohanta, J., & Dey, B. (2021). *European Journal of Advanced Chemistry Research*, 1. <https://doi.org/10.24018/ejchem.2022.3.1.82>
- Farag, A. M., Sokker, H. H., Zayed, E. M., Nour Eldien, F. A., & Abd Alrahman, N. M. (2018). *International Journal of Biological Macromolecules*, 120, 2188. <https://doi.org/10.1016/j.ijbiomac.2018.06.171>
- Haq, F., Yu, H., Wang, Y., Wang, L., Haroon, M., Khan, A., Mehmood, S., & Lin, T. (2020). *Journal of Molecular Structure*, 1207, 127752. <https://doi.org/10.1016/j.molstruc.2020.127752>
- Hashem, A., Abdel-Halim, E. S., & Sokker, H. H. (2007). *Polymer-Plastics Technology and Engineering*, 46, 71. <https://doi.org/10.1080/03602550600950364>
- He, X., Du, M., Li, H., & Zhou, T. (2016). *Journal of Biological Macromolecules*, 82, 174. <https://doi.org/10.1016/j.ijbiomac.2015.11.005>
- Hosseinzadeh, H., & Ramin, S. (2018). *International Journal of Biological Macromolecules*, 106, 101. <https://doi.org/10.1016/j.ijbiomac.2017.07.182>
- Irinislimane, H., & Belhaneche-Bensemra, N. (2017). *Chemical Engineering Communications*, 204, 897. <https://doi.org/10.1080/00986445.2017.1325739>
- Jiang, R., Zhu, H. Y., Li, J. B., Fu, F. Q., Yao, J., Jiang, S. T., & Zeng, G. M. (2016). *Applied Surface Science*, 364, 604. <https://doi.org/10.1016/j.apsusc.2015.12.200>
- Jiang, S., Yu, Z., Hu, H., Lv, J., Wang, H., & Jiang, S. (2017). *Journal of Food Science and Technology*, 84, 10. <https://doi.org/10.1016/j.jwt.2017.05.047>
- Junlapong, K., Maijan, P., Chaibundit, C., & Chantarak, S. (2020). *International Journal of Biological Macromolecules*, 158, 258. <https://doi.org/10.1016/j.ijbiomac.2020.04.247>
- Kumari, R., & Dey, S. (2019). *Desalination and Water Treatment*, 158, 319. <https://doi.org/10.5004/dwt.2019.24223>
- Kumari, R., Mohanta, J., Dey, B., & Dey, S. (2020). *Separation Science and Technology*, 55, 3047. <https://doi.org/10.1080/01496395.2019.1670208>
- Kumari, R., Khan, M. A., Mahto, M., Qaiyum, M. A., Mohanta, J., Dey, B., & Dey, S. (2020b). *ACS Omega*, 5, 19548. <https://doi.org/10.1021/acsomega.0c02011>
- Li, P., Gao, B., Li, A., & Yang, H. (2018a). *Microporous and Mesoporous Materials*, 263, 210. <https://doi.org/10.1016/j.micromeso.2017.12.025>
- Li, C., Lou, T., Yan, X., Long, Y.-Z., Cui, G., & Wang, X. (2018). *International Journal of Biological Macromolecules*, 106, 768. <https://doi.org/10.1016/j.ijbiomac.2017.08.072>
- Li, P., Gao, B., Li, A., & Yang, H. (2020). *International Journal of Biological Macromolecules*, 149, 1285. <https://doi.org/10.1016/j.ijbiomac.2020.02.047>
- Liu, M., Huang, H., Wang, K., Xu, D., Wan, Q., Tian, J., Huang, Q., Deng, F., Zhang, X., & Wei, Y. (2016). *Carbohydrate Polymers*, 142, 38. <https://doi.org/10.1016/j.carbpol.2016.01.030>
- Ma, D., Zhu, B., Cao, B., Wang, J., & Zhang, J. (2017). *Applied Surface Science*, 422, 944. <https://doi.org/10.1016/j.apsusc.2017.06.072>
- Mahmoud, M. E., Nabil, G. M., Zaki, M. M., & Saleh, M. M. (2019). *International Journal of Biological Macromolecules*, 137, 455. <https://doi.org/10.1016/j.ijbiomac.2019.06.170>
- Mallakpour, S., & Rashidimoghadam, S. (2017). *Carbohydrate Polymers*, 169, 23. <https://doi.org/10.1016/j.carbpol.2017.03.081>
- Mittal, H., Alhassan, S. M., & Ray, S. S. (2018). *Journal of Environmental Chemical Engineering*, 6, 7119. <https://doi.org/10.1016/j.jece.2018.11.010>
- Mittal, H., Alhassan, S. M., & Ray, S. S. (2018). *Journal of Environmental Chemical Engineering*, 6, 7119. <https://doi.org/10.1016/j.jece.2018.11.010>
- Mohanta, J., Dey, B., & Dey, S. (2020a). *Desalination and Water Treatment*, 189, 227. <https://doi.org/10.5004/dwt.2020.25570>
- Mohanta, J., Dey, B., & Dey, S. (2020). *Journal of Chemical & Engineering Data*, 65, 2819. <https://doi.org/10.1021/acs.jced.0c00131>
- Mohanta, J., Dey, B., & Dey, S. (2020). *ACS Omega*, 5, 16510. <https://doi.org/10.1021/acsomega.0c00999>
- Mohanta, J., Xalxo, R., & Dey, S. (2019). Efficient Removal of Malachite Green from Contaminated Water using Pyro-lusite. *Green Energy & Efficient Technology mateials*. U.K.: LAP Lambert Academic Publishers (Cambridge Scholar).
- Moharrami, P., & Motamedi, E. (2020). *Bioresource Technology*, 313, 123661. <https://doi.org/10.1016/j.biortech.2020.123661>
- Muthukumar, C., Sivakumar, V. M., & Thirumarimurugan, M. (2016). *Journal of the Taiwan Institute of Chemical Engineers*, 63, 354. <https://doi.org/10.1016/j.jtice.2016.03.034>
- Muzaffar, S., & Tahir, H. (2018). *Journal of Molecular Liquids*, 252, 368. <https://doi.org/10.1016/j.molliq.2018.01.007>
- Namazi, H., Hasani, M., & Yadollahi, M. (2019). *International Journal of Biological Macromolecules*, 126, 578. <https://doi.org/10.1016/j.ijbiomac.2018.12.242>
- Naushad, M., Allothman, Z. A., Awwal, M. R., Alfadul, S. M., & Ahamad, T. (2016). *Desalination and Water Treatment*, 57, 13527. <https://doi.org/10.1080/19443994.2015.1060169>
- Noreen, S., Bhatti, H. N., Iqbal, M., Hussain, F., & Sarim, F. M. (2020). *International Journal of Biological Macromolecules*, 147, 439. <https://doi.org/10.1016/j.ijbiomac.2019.12.257>
- Nsom, M. V., Etape, E. P., Tendo, J. F., Namond, B. V., Chongwain, P. T., Yufanyi, M. D., & William N. (2019). *Journal of Nanomaterials*, 1. <https://doi.org/10.1155/2019/4576135>
- Pourjavadi, A., Abedin-Moghanaki, A., & Tavakoli, A. (2016). *RSC Advances*, 6, 38042. <https://doi.org/10.1039/c6ra02517j>

- Priyanka, M., & Saravanakumar, M. P. (2018). *Journal of Cleaner Production*, 197, 511. <https://doi.org/10.1016/j.jclepro.2018.06.197>
- Qaiyum, M. A., Kumari, R., Mohanta, J., Samal, P. P., Dey, B., & Dey, S. (2022). *Journal of Cluster Science*. <https://doi.org/10.1007/s10876-022-02270-1>
- Saad, M., Tahir, H., Khan, J., Hameed, U., & Saud, A. (2017). *Ultrasonics Sonochemistry*, 34, 600. <https://doi.org/10.1016/j.ultsonch.2016.06.022>
- Sarmah, D., & Karak, N. (2020). *Carbohydrate Polymers*, 242, 116320. <https://doi.org/10.1016/j.carbpol.2020.116320>
- Sharifpour, E., Ghaedi, M., Asfaram, A., Farsadrooh, M., Dil, E. A., & Javadian, H. (2020). *International Journal of Biological Macromolecules*, 152, 913. <https://doi.org/10.1016/j.ijbiomac.2020.02.236>
- Sharma, A., Sharma, G., Kumar, A., Siddiqi, Z. M., & Pathania, D. (2016). *Materials Science Forum*, 875, 1. <https://doi.org/10.4028/www.scientific.net/MSF.875.1>
- Sharma, G., Naushad, M., Pathania, D., & Kumar, A. (2016). *Desalination and Water Treatment*, 57, 19443. <https://doi.org/10.1080/19443994.2015.1096834>
- Sharma, G., AlOthman, Z. A., Kumar, A., Sharma, S., Ponusamy, S. K., & Naushad, M. (2017). *Nanotechnology for Environmental Engineering*, 2, 1. <https://doi.org/10.1007/s41204-017-0014-y>
- Sharma, A., Siddiqi, Z.-M., & Pathania, D. (2017). *Journal of Molecular Liquids*, 240, 361. <https://doi.org/10.1016/j.molliq.2017.05.083>
- Sharma, G., Thakur, B., Naushad, M., Al-Muhtaseb, A. H., Kumar, A., Sillanpaa, M., & Mola, G. T. (2017a). *Materials Chemistry and Physics*, 193, 129–139. <https://doi.org/10.1016/j.matchemphys.2017.02.010>
- Sharma, G., Naushad, M., Kumar, A., Rana, S., Sharma, S., Bhatnagar, A., Stadler, F. J., Ghfar, A. A., & Khan, M. R. (2017b). *Process Safety and Environment Protection*, 109, 301. <https://doi.org/10.1016/j.psep.2017.04.011>
- Sharma, A., Sharma, G., Naushad, M., Ghfar, A. A., & Pathania, D. (2017). *Environmental Technology*, 39, 1. <https://doi.org/10.1080/09593330.2017.1317293>
- Sharma, G., Kumar, A., Devi, K., Sharma, S., Naushad, M., Ghfar, A. A., Ahamad, T., & Stadler, F. J. (2018). *International Journal of Biological Macromolecules*, 114, 295. <https://doi.org/10.1016/j.ijbiomac.2018.03.093>
- Sharma, A., Thakur, K. K., Mehta, P., & Pathania, D. (2018). *Sustainable Chemistry and Pharmacy*, 9, 1. <https://doi.org/10.1016/j.scp.2018.04.002>
- Sharma, A., Siddiqi, Z. M., Dhar, S., Mehta, P., & Pathania, D. (2019). *Separation Science and Technology*, 54, 916. <https://doi.org/10.1080/01496395.2018.1524908>
- Shehzad, K., Ahmad, M., Xie, C., Zhan, D., Wang, W., Li, Z., Xu, W., & Liu, J. (2019). *Journal of Hazardous Materials*, 373, 75. <https://doi.org/10.1016/j.jhazmat.2019.01.021>
- Sonawane, R. O., & Patil, S. D. (2018). *International Journal of Biological Macromolecules*, 120, 2324. <https://doi.org/10.1016/j.ijbiomac.2018.08.177>
- Stan, M., Lung, I., Soran, M. L., Opris, O., Leostean, C., Popa, A., Copaciu, F., Lazar, M. D., Kacso, I., Silipas, T. D., & Porav, A. S. (2019). *Data Brief*, 25, 104165. <https://doi.org/10.1016/j.dib.2019.104165>
- Su, X., Xiao, C., & Hu, C. (2018). *International Journal of Biological Macromolecules*, 115, 1189. <https://doi.org/10.1016/j.ijbiomac.2018.04.060>
- Sukriti, S., Sharma, J., Pruthi, V., Anand, P., Chaddha, A. P. S., Bhatia, J., & Kaith, B. S. (2016). *RSC Advances*, 6, 74300. <https://doi.org/10.1039/c6ra12715k>
- Tao, X., Liu, D., Cong, W., & Huang, L. (2018). *Applied Surface Science*, 457, 572. <https://doi.org/10.1016/j.apsusc.2018.06.264>
- Xia, W., Zheng, B., Li, T., Lian, F., Lin, Y., & Liu, R. (2020). *Carbohydrate Polymers*, 250, 116848. <https://doi.org/10.1016/j.carbpol.2020.116848>
- Xing, G., Liu, S., Xu, Q., & Liu, Q. (2012). *Carbohydrate Polymers*, 87, 1447. <https://doi.org/10.1016/j.carbpol.2011.09.038>
- Yang, X., Jin, D., Zhang, M., Wu, P., Jin, H., Li, J., Wang, X., Ge, H., Wang, Z., & Lou, H. (2016). *Materials Chemistry and Physics*, 174, 179. <https://doi.org/10.1016/j.matchemphys.2016.02.073>
- Zain, G., Nada, A. A., El-Sheikh, M. A., Attaby, F. A., & Waly, A. I. (2018). *International Journal of Biological Macromolecules*, 115, 61. <https://doi.org/10.1016/j.ijbiomac.2018.04.032>
- Zare, E. N., Motahari, A., & Sillanpää, M. (2018). *Environmental Research*, 162, 173. <https://doi.org/10.1016/j.envres.2017.12.025>
- Zhang, H., Tang, Y., Liu, X., Ke, Z., Su, X., Cai, D., Wang, X., Liu, Y., Huang, Q., & Yu, Z. (2011). *Desalination*, 274, 97. <https://doi.org/10.1016/j.desal.2011.01.077>
- Zhang, H., Zhang, F., & Huang, Q. (2017). *RSC Advances*, 7, 5790. <https://doi.org/10.1039/c6ra27782a>
- Zhang, H., Li, Y., Cheng, B., Ding, C., & Zhang, Y. (2020). *International Journal of Biological Macromolecules*, 161, 561. <https://doi.org/10.1016/j.ijbiomac.2020.06.017>
- Zhou, Z., Du, H., Dai, Z., Mu, Y., Tong, L., Xing, Q., Liu, S. S., Ao, Z., & Zou, J. P. (2019). *Chemical Engineering Journal*, 374, 170. <https://doi.org/10.1016/j.cej.2019.05.170>

Publisher's Note Springer Nature remains neutral with regard to jurisdictional claims in published maps and institutional affiliations.

Springer Nature or its licensor (e.g. a society or other partner) holds exclusive rights to this article under a publishing agreement with the author(s) or other rightsholder(s); author self-archiving of the accepted manuscript version of this article is solely governed by the terms of such publishing agreement and applicable law.